BL16XU
SUNBEAM ID

1. Introduction

BL16XU, which is referred to as SUNBEAM ID, together with its sister beamline BL16B2, was built to develop various industrial materials by utilizing the high-brightness beam at the large-scale synchrotron radiation facility in SPring-8. It is operated by the SUNBEAM Consortium, which is a private organization comprising 13 companies* (12 firms and one electric power group). BL16XU and BL16B2 began operations in September 1999, and the beamline use contract was renewed in April 2018. In August 2020, we received an interim evaluation and obtained a "continuation" evaluation result.

X-rays emitted from an undulator are monochromatized, shaped, and converged in an optics hutch. The experimental hutch contains four experimental devices. Figure 1 and Table 1 schematically depict and outline the characteristics of BL16XU, respectively.

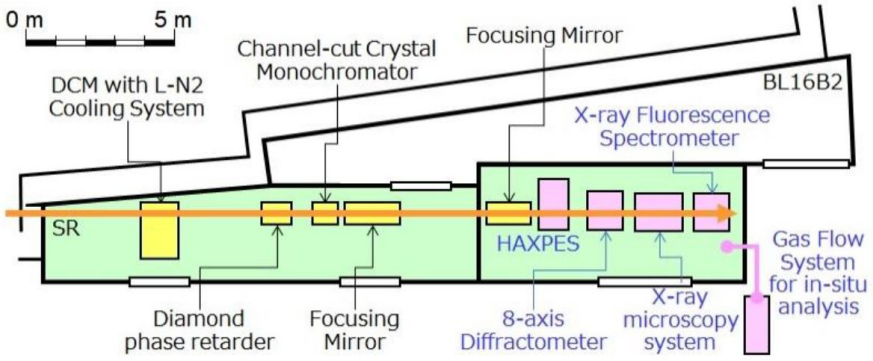

Fig. 1. Outline of BL16XU.

Table 1. Characteristics of BL16XU.

Light source	in-vacuo X-ray undulator λ = 40 mm, N = 112
Energy range	4.5–40 keV
Energy resolution ($\Delta E/E$)	~10^{-4}
Photon intensity, beam size	~10^{12} photons/s, < 1 mm × 1 mm ~10^{10} photons/s, < 500 nm × 500 nm
Beam position stability	±0.1 mm horizontal ±0.8 mm vertical (5.0–30 keV)
Experimental facilities	HAXPES, XRD, XRF, Microbeam (Microscopy), Gas flow system (corrosive or toxic gas is possible)

*Kawasaki Heavy Industry, Ltd., Kobe Steel, Ltd., Sumitomo Electric Industries, Ltd., Sony Group Corp., Electric power group (Kansai Electric Power Co., Inc., Central Research Institute of Electric Power Industry), Toshiba Corp., Toyota Central R&D Labs., Inc., Nichia Corp., Nissan Motor Co., Ltd., Panasonic Holdings Corp., Hitachi, Ltd., Fujitsu, Ltd., Mitsubishi Electric Corp.

2. Utilization

Figure 2 shows the utilization of BL16XU in the past decade. The vertical axis shows the proportions of users, excluding the tuning and studying of the beamline itself. The upper graph depicts the utilization by field. The application fields are mainly semiconductors, batteries, and materials. In recent years, research related to green innovations, such as lithium-ion batteries, fuel cells, SiC, and GaN, has been progressing.

The lower graph shows the utilization of equipment (technology). The utilization of hard X-ray photoelectron spectroscopy (HAXPES) equipment, which was installed in 2014, is increasing. HAXPES is mainly used for semiconductors and battery materials.

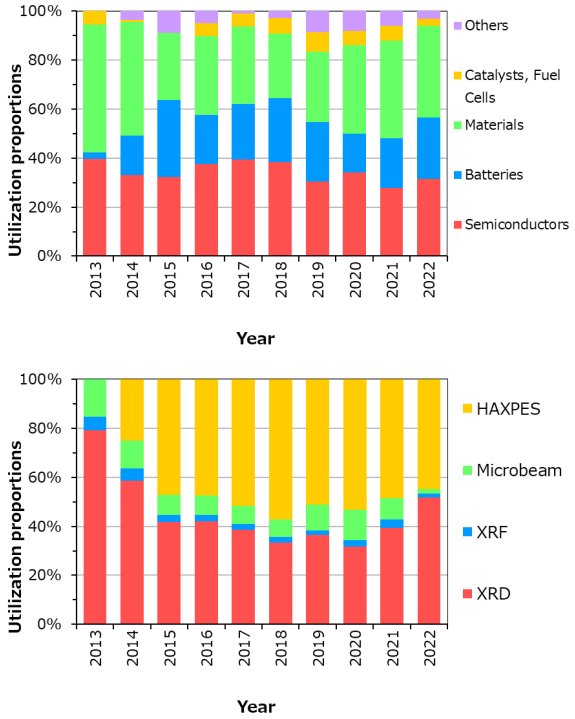

Fig. 2. Relative utilization times of BL16XU in the past decade.

3. Topics in FY2022

Below, the research and upgrades conducted in FY2022 are described.

3-1. Three-dimensional micro-X-ray topography using focused sheet-shaped X-ray beam [1]

X-ray topography is a powerful method for analyzing crystal defects and strain in crystalline materials nondestructively. However, conventional X-ray topography uses simple X-ray diffraction images, which means that depth information of defects and dislocations cannot be obtained. We have therefore developed a novel three-dimensional micro-X-ray topography technique (3D μ-XRT) that is a combination of Bragg-case section topography with focused sheet-shaped X-rays. The depth resolution of the 3D μ-XRT depends mainly on the focused X-ray beam size and enables the nondestructive observation of internal defects and dislocations with an accuracy on the order of 1 μm.

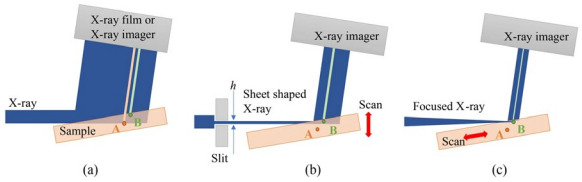

Fig. 3. Schematic view of (a) conventional reflection topography (Bragg-case), (b) reflection section topography, and (c) the proposed 3D μ-XRT using a sheet-shaped focused X-ray beam [1].

The X-ray beam is focused separately in the vertical and horizontal directions by two total-reflection mirrors in a Kirkpatrick–Baez (KB) optical configuration at the beamline BL16XU. Therefore, a one-dimensional focused X-ray is obtained by retracting one mirror from the optical beam path, as shown in Fig. 3(c) (in this case, the

horizontal focusing mirror was retracted). Note that if the sample is scanned up and down vertically, as in conventional section topography, the focal point and the sample irradiation position will be misaligned. Therefore, the sample was scanned parallel to the surface so that the focal point of the X-ray beam and the sample irradiation point always coincide, as shown in Fig. 3(c).

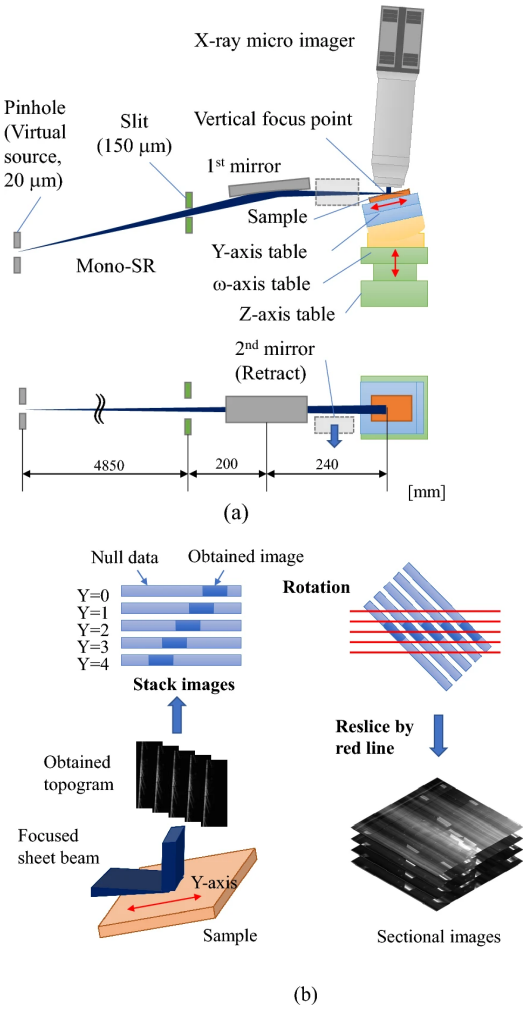

Fig. 4. (a) Schematic view of 3D μ-XRT system constructed at BL16XU and (b) image processing procedure [1].

We designed the 3D μ-XRT system using the microbeam system [2] installed at beamline BL16XU. As shown in Fig. 4(a), the system consists of a focusing mirror, a sample positioner, and an X-ray micro-imager. Note that a second focusing mirror for the horizontal direction is retracted from the optical beam path to form a sheet-shaped X-ray beam in this optical configuration. The reduction ratio is approximately 1/20, and the X-ray beam can be focused to 1 μm by setting the pinhole vertical aperture to 20 μm. We also set the vertical aperture of the slit to 150 μm, and reduced the vertical divergence angle of the SR irradiating the sample to 0.6 mrad, which is sufficiently wide compared with the diffraction width of the sample. Therefore, the image contrast was dominated by kinematic diffraction. Each topogram was acquired at the maximum diffraction intensity angle using a scanning ω-table. A lens-coupled X-ray imager (Rad device, Xsight Micron™) is used as the X-ray micro-imager. The incident X-rays are converted to visible light by a phosphor and then imaged onto an sCMOS visible camera (Andor Zyla, pixel size: 6.5 μm, 2048 × 2048 pixels) by the visible light lens system. We utilize a 5 × objective lens with a pixel size of 1.3 μm and a field of view of 2.6 mm^2. Obtained topograms are shifted when scanning the sample along the Y-axis [as shown in Fig. 4(b)], so we reconstruct a standard 3D topogram with a ratio of 1:1:1 and orthogonally intersect each axis by shifting, stacking, and rotating each topogram using SAKAS-Viewer [3] and Image J.

We conducted a feasibility test of the 3D μ-XRT using the monochromatic SR of 1.0 μm and 2 mm in the vertical and horizontal directions, respectively. SiC (2-2010) X-ray diffraction of a 4H-SiC power device chip (3.3-kV double-implanted SiC MOSFET [4]) consisting of a 30-μm-thick epitaxial layer on the surface and 4°-off-cut (0001) was used. The SR energy was set to 10.5 keV, the calculated incident angle (ω) was 10.2 degrees, the exit angle

(2θ) was 84.3 degrees, and the X-ray penetration depth was 40 μm. The sample was scanned along the sample surface (Y-axis) with 2.5 μm steps. The number of scanning points was 3500, each topogram was acquired with an exposure time of 2 s, and the total measurement time was about 2 h.

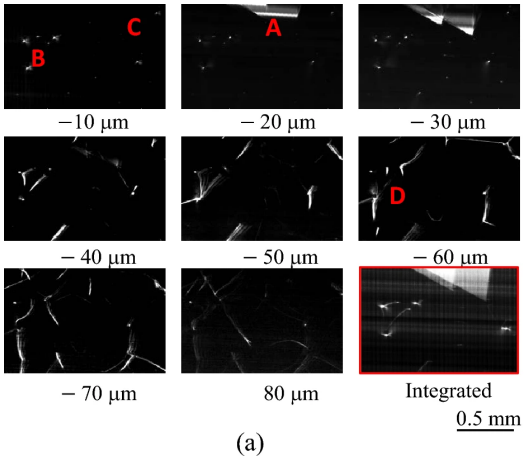

(a)

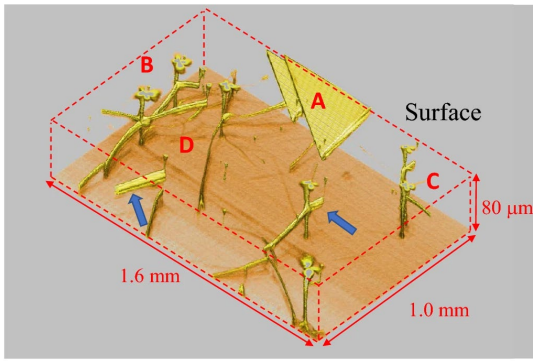

(b)

Fig. 5. (a) Cross-sectional topogram of a SiC chip every 10 μm from the surface and integrated sectional topograms from the surface to 40 μm depth (lower-right). (b) 3D topogram [1].

Figure 5(a) shows cross-sectional topograms every 10 μm from the surface and Fig. 5(b) shows a 3D volume rendering topogram of the same area. Stacking faults (A) in the epitaxial layer, basal plane dislocations (BPD) under the epitaxial layer (D), and threading screw (TSD) and threading edge (TED) dislocations (B, C) penetrating the layer are clearly visualized in both figures. The complex connections between the BPD, TSD, and TED, as well as the BPD → SF and BPD → TED conversions [5], [6], were also clearly observed near the boundary between the epitaxial layer and the substrate. The three-dimensional curvature of the BPD, which provides important thermal information for the fabrication process, can also be clearly visualized. Note that some BPDs have sub-fringes and blurring (blue arrows). This blurring might be caused by the Pendellösung fringes in the Bragg case [7], [8].

3D μ-XRT is a promising new approach for the highly sensitive and nondestructive analysis of material crystallinity in a three-dimensional manner.

Sakaki Atsushi
SUNBEAM Consortium
NICHIA CORPORATION

References:

[1] Yoneyama, A. et al. (2023). *Sci. Rep.* **13**, 12381.
[2] Hirai, Y. et al. (2004). *Nucl. Instrum. Methods Phys. Res. Sect. A* **521**, 538–548.
[3] Yoneyama, A. et al. (2023) in *European Congress of Radiology (ECR)*.
[4] Konishi, K. et al. (2021). *J. Appl. Phys.* **130**, 145703.
[5] Ha, S. et al. (2002). *J. Cryst. Growth* **244**, 257–266.
[6] Zhang, Z. et al. (2005). *Appl. Phys. Lett.* **87**, 151913.
[7] Uragami, T. S. et al. (1970). *J. Phys. Soc. Jpn.* **28**, 1508–1527.
[8] Saka, T. et al. (1973). *Acta Crystallogr. Sect. A* **29**, 192–200.